AIAA SciTech Forum
11–15 & 19–21 January 2021, VIRTUAL EVENT
AIAA Scitech 2021 Forum

10.2514/6.2021-0731

Adaptive Mesh Refinement for Fluid-Structure Interaction Simulations

Vivek Ojha*, Krzysztof J. Fidkowski†, and Carlos E. S. Cesnik‡
Department of Aerospace Engineering, University of Michigan, Ann Arbor, MI 48109, USA

This paper introduces an adaptive mesh refinement approach for solving fluid-structure interaction problems. A high-order partitioned approach is applied to couple the fluid and the structural subsystems, where the fluid subsystem is discretized using a discontinuous Galerkin finite-element method, while the structural solver uses a continuous Galerkin discretization. The space-time mesh of the fluid subsystem is adapted using a goal-oriented approach based on the coupled adjoint. Error estimates for unsteady outputs are evaluated using an adjoint-weighted residual after calculating the unsteady adjoint of the coupled system. The benefits of adaptive meshing are demonstrated on fluid and structural outputs of interest evaluated for a two-dimensional pitching-plunging airfoil in a high-Reynolds number flow and a cantilever beam in a laminar flow.

I. Introduction

The interaction between a movable or deformable structure with an internal or surrounding fluid flow, generally referred to as fluid-structure interaction (FSI), finds relevance across various disciplines of engineering. The field of aeroelasticity is one such field where FSI plays a crucial role. Accurate numerical simulation of the interaction between the elastic wing of an airplane and the incoming flow is important for understanding, for example, performance and aeroservoelastic stability and response predictions. High-fidelity computational aeroelasticity (CAE) solves the complete Navier-Stokes equations using computational fluid dynamics (CFD) coupled with the finite element modeling of the structure using computational structural dynamics (CSD). These high-fidelity models have the capability to capture nonlinearities in the flow as well as in the structure. High fidelity is also critical in the transonic regime where complex phenomena exist such as buffeting, buzz, and flutter "transonic dip".[1] The interaction between the fluid and structural subsystems involves multiple scales, thereby making the coupled system challenging to solve. Many numerical approaches have been suggested for simulating fluid-structure interaction[2] and these can be broadly divided into two categories: monolithic and partitioned. The monolithic approach[3] is a fully-coupled approach where the two systems are solved simultaneously. This approach combines both systems into one large system of equations and solves them simultaneously, which often leads to accurate results but requires significant implementation effort and uses less efficient solvers. The second approach, generally referred to as the partitioned approach, uses two separate solvers to solve the subsystems and then couples them by communication between the solvers. This method facilitates software modularity and mathematical modeling. The present work implements a high-order partitioned approach based on the implicit explicit Runge Kutta scheme (IMEX) presented in the work of Van Zuijlen et al.,[4] which couples the two subsystems without sub-iterations.

Accurate evaluation of functional outputs of interest in high-fidelity aeroelasticity is challenging because of the substantial computational effort involved. Increasing the accuracy of outputs from coupled simulations using heuristic approaches such as uniform space-time mesh refinement makes the simulation computationally expensive and inefficient. Finite-element techniques employing goal-oriented adaptive strategies can offer significant efficiency improvements. They offer a systematic approach for identifying regions of the domain

*Ph.D. Candidate, AIAA Student Member
†Associate Professor, AIAA Senior Member
‡Clarence L. "Kelly" Johnson Collegiate Professor of Aerospace Engineering, AIAA Fellow

that require more resolution for the prediction of outputs of interest.[5]

Goal-oriented mesh adaptation techniques rely on local error indicators. These indicators depend on the sensitivity information which is obtained in the form of solutions to the adjoint problem. A comprehensive analysis of the linearized adjoint formulation for coupled FSI problems is given by van der Zee et al.[6] In that work, the domain-map linearization approach is used to obtain the adjoint, where the fluid sub-problem is first transformed to a fixed reference domain, after which one linearizes with respect to the domain transformation map.

In this paper, a coupled adjoint is developed for a high-order FSI solver. Further, goal-oriented mesh adaption in the fluid subsystem is developed using the coupled adjoint and is applied to two-dimensional FSI cases to demonstrate a benefit in accuracy and a reduction in computational cost. The outline of the remainder of the paper is as follows. Section II reviews the governing equations of the fluid and structural subsystems. Section III reviews the spatial and temporal coupling algorithm for the partitioned approach. Section IV reviews the error estimation and mesh adaptation strategies used in this work. Finally, Section V outlines the results generated using these methods.

II. Governing Equations

II.A. Fluid Subsystem

The fluid subsystem is governed by the Navier-Stokes equations, given by

$$\frac{\partial \mathbf{u}}{\partial t}\Big|_x + \nabla \cdot \vec{\mathbf{F}}(\mathbf{u}, \nabla \mathbf{u}) = \mathbf{0}, \quad \vec{\mathbf{F}} = \vec{\mathbf{F}}^i(\mathbf{u}) - \vec{\mathbf{F}}^v(\mathbf{u}, \nabla \mathbf{u}), \tag{1}$$

where $\mathbf{u}(\vec{x}, t) \in \mathbb{R}^{\hat{s}}$ is the conservative state vector, $\vec{x} \in \mathbb{R}^d$ is the spatial coordinate, $t \in \mathbb{R}$, d is the number of space dimensions, and $\vec{\mathbf{F}}^i$ and $\vec{\mathbf{F}}^v$ are the inviscid and viscous fluxes, respectively. In the case of a non-deformable domain, the fluid equations are solved numerically in the Eulerian reference frame, where the computational grid is fixed and the fluid moves with respect to the grid. However, numerical simulation of fluid dynamics involving a deforming domain, such as in the case of FSI, faces issues due to the lack of a precise interface definition and under-resolved flow features when solved in the Eulerian frame of reference. Alternatively, the Lagrangian approach, in which each node in the fluid mesh follows the material particle during motion, faces problems dealing with large distortions of the computational domain. To resolve these issues, an alternate method, the Arbitrary Lagrangian Eulerian approach, is employed in the present work.

II.B. Arbitrary Lagrangian-Eulerian Formulation

The Arbitrary Lagrangian-Eulerian (ALE) formulation combines advantages of both the Eulerian and Lagrangian approaches. In this method, the deformable physical domain is mapped to a fixed referenced domain by a time-dependent mapping. A simple and effective ALE method for DG was introduced by Persson et al.[7] and a similar approach is followed in this work.[8]

Let $\vec{x} = \mathscr{G}(\vec{X}, t)$ represent the one-to-one time-dependent mapping between the physical volume and the reference volume. Each point $\vec{X}$ in the static reference domain is mapped to a corresponding point $\vec{x}$ in the physical domain, based on the desired deformation of the mesh. The spatial Jacobian of the mapping, represented by the d×d matrix $\underline{G}$, and the mapping velocity, $\vec{v}_X$, are given by

$$\underline{G} = \nabla_X \mathscr{G}, \quad \vec{v}_X = \frac{\partial \mathscr{G}}{\partial t}\Big|_X. \tag{2}$$

Let g=det($\underline{\mathrm{G}}$). The corresponding Navier-Stokes equations in the reference frame can be written as

$$\frac{\partial \mathbf{u}_X}{\partial t}\Big|_X + \nabla_X \cdot \vec{\mathbf{F}}_X(\mathbf{u}_X, \nabla_X \mathbf{u}_X) = \mathbf{0}, \quad \vec{\mathbf{F}}_X = \vec{\mathbf{F}}^i_X(\mathbf{u}_X) - \vec{\mathbf{F}}^\nu_X(\mathbf{u}_X, \nabla_X \mathbf{u}_X), \tag{3}$$

where the transformed vectors, derivatives, and fluxes in the reference frame are given by:

$$\mathbf{u}_X = g\mathbf{u}, \tag{4}$$

$$\nabla_x \mathbf{u} = \nabla_X (g^{-1}\mathbf{u}_X)\underline{G}^{-T} = (g^{-1}\nabla_X \mathbf{u}_X - \mathbf{u}_X \nabla_X (g^{-1}))\underline{G}^{-T}, \tag{5}$$

$$\vec{\mathbf{F}}^i_X = g\underline{G}^{-1}\vec{\mathbf{F}}^i - \mathbf{u}_X \underline{G}^{-1}\vec{v}_X, \qquad \vec{\mathbf{F}}^\nu_X = g\underline{G}^{-1}\vec{\mathbf{F}}^\nu. \tag{6}$$

II.C. Spatial Discretization

To discretize the state equations (Eq. 1), a discontinuous Galerkin finite-element method is used in space.[9–11] DG, as a finite-element method, approximates the state $\mathbf{u}$ in functional form using linear combinations of basis functions on each element. No continuity constraints are imposed between adjacent elements. Denoting by T_h the set of N_e elements in a non-overlapping tessellation of the domain Ω, the state on element e, Ω_e, is approximated as

$$\mathbf{u}_h(\vec{x}(\vec{\xi}))\Big|_{\Omega_e} = \sum_{n=1}^{N_p} \mathbf{U}_{en}\phi_{en}(\vec{x}(\vec{\xi})). \tag{7}$$

In this equation, N_p is the number of basis functions per element, $\mathbf{U}_{en}$ is the vector of s coefficients for the n^{th} basis function on element e: $\phi_{en}(\vec{x}(\vec{\xi}))$, and s is the state rank. $\vec{x}$ denotes the global coordinates, and $\vec{\xi}$ denotes the reference-space coordinates in a master element. Formally, $\mathbf{u}_h \in \boldsymbol{\mathcal{V}}_h = [\mathcal{V}_h]^s$, where, if the elements are not curved, $\mathcal{V}_h = \{u \in L_2(\Omega) : u|_{\Omega_e} \in \mathcal{P}^p \ \forall \Omega_e \in T_h\}$, and $\mathcal{P}^p$ denotes polynomials of order p on the element. With the spatial discretization described above, the governing equations can written in an abbreviated form as:

$$\bar{\mathbf{R}}^f = \mathbf{M}^f \frac{\mathrm{d}\mathbf{U}^f}{\mathrm{d}t} - \mathbf{r}^f = \mathbf{0}, \tag{8}$$

where $\mathbf{r}^f$ is the discrete spatial residual vector, $\mathbf{M}^f$ is the fluid mass matrix, $\bar{\mathbf{R}}^f$ is the temporally strong-form unsteady residual, and the f superscript denotes that these equations apply to the fluids subsystem.

II.D. Structural Subsystem

The structural dynamics are governed by a set of partial differential equations with an arbitrary constitutive law. For the initial development of the coupled solver, a linear structural model is assumed. Discretizing the governing equations in space using a (continuous) finite-element method, the equations are given by:

$$\bar{\mathbf{M}}\ddot{\mathbf{u}}^s + \mathbf{C}\dot{\mathbf{u}}^s + \mathbf{K}\mathbf{u}^s = \mathbf{F}, \tag{9}$$

where $\mathbf{u}^s$ represents the vector of displacements, $\bar{\mathbf{M}}$ is the mass matrix, and $\mathbf{K}$ is the stiffness matrix. $\mathbf{C}$ denotes the damping in the structure, and $\mathbf{F}$ represents the vector of external forces acting on the structure. The second-order form of the equilibrium equations, Eq. 9, can be re-written in first order as:

$$\begin{bmatrix} \bar{\mathbf{M}} & \mathbf{0} \\ \mathbf{0} & \mathbf{1} \end{bmatrix} \dot{\mathbf{U}}^s + \begin{bmatrix} \mathbf{C} & \mathbf{K} \\ \mathbf{-1} & \mathbf{0} \end{bmatrix} \mathbf{U}^s = \begin{bmatrix} \mathbf{0} \end{bmatrix}, \quad \text{where} \quad \mathbf{U}^s = \begin{bmatrix} \dot{\mathbf{u}}^s \\ \mathbf{u}^s \end{bmatrix}, \tag{10}$$

and $\mathbf{1}$ denotes the identity matrix. Finally, the governing equations can be written in an abbreviated form as:

$$\bar{\mathbf{R}}^s = \mathbf{M}^s \frac{\mathrm{d}\mathbf{U}^s}{\mathrm{d}t} - \mathbf{r}^s = \mathbf{0}, \tag{11}$$

where $\mathbf{r}^s$ is the discrete spatial residual vector, $\mathbf{M}^s$ is the augmented mass matrix, and $\bar{\mathbf{R}}^s$ is the strong-form unsteady residual. The superscript s denotes that these equations apply to the structures subsystem.

III. Fluid-Structure Coupling

III.A. Spatial Coupling

The partitioned approach for FSI allows to use a separate mesh discretization for each subsystem, which offers the advantage of resolving regions of complex flow in the fluids or large displacement in the structures. This may result in meshes for the coupled problem which may not share coincident node locations at the interface. Thus, a spatial coupling algorithm is required to interpolate interface displacement and velocities from the structural mesh to the fluids, and loads from the fluid mesh to the structures. Radial basis functions (RBF) provide high accuracy for interpolation and have been used for the spatial coupling in this work.[12]

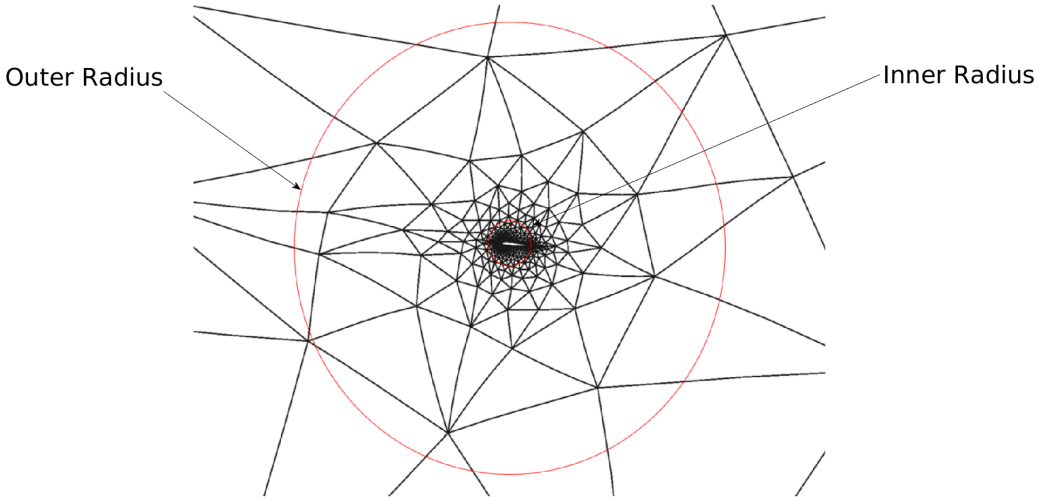

Figure 1: Example of inner and outer radius of the blending region for the explicit mapping mesh motion.

III.B. Mesh Deformation

For deforming domains, the ALE formulation of the Navier-Stokes equations requires a mapping between the reference and the deformed physical mesh. The mapping interpolates the boundary displacements to the interior of the fluid mesh. The explicit mapping presented by Persson et al.[13] does not require solving a system of equations for deforming the volume. It uses explicit expressions for the mapping that blend the motion, smoothly reducing it to the identity mapping away from the boundary. For any rigid body deformation, the mesh motion algorithm divides the entire spatial domain into two regions based on inner and outer radii of the blending region. The region extending up to the inner radius from the center of the deformation marks the region of rigid deformation. Within this region, any deformation provided by the user is applied to all of the mesh elements without any blending. The presence of the rigid region prevents errors such as mesh element inversion in highly-stretched elements, which face such errors when placed in a blending region. The blending region, which exists between the inner and outer radii from the center of the motion, uses a polynomial function to blend the deformation radially such that the deformation goes to zero at the outer radius. To achieve blending of the motion, septic polynomial blending functions,

$$P(r) = -20r^7 + 70r^6 - 84r^5 + 35r^4, \tag{12}$$

are used, where r is the normalized radial distance from the inner radius. Figure 1 shows the deformed mesh for an airfoil undergoing rigid-body pitch motion. The inner and outer radii are placed at one and ten chords away, respectively, from the center of motion, which is at the quarter chord of the airfoil. For the cantilever beam considered in the later part of this work, RBFs are used to deform the fluid mesh. In this work, a compact C^0 continuous basis function based on a polynomials with a support radius of one chord is used.[14]

III.C. IMEX

The coupled FSI problem can be represented in semi-discrete form as

$$\mathbf{M}\dot{\mathbf{u}} = \mathbf{r}(\mathbf{u}), \tag{13}$$

$$\mathbf{u} = \begin{bmatrix} \mathbf{u}^f \\ \mathbf{u}^s \end{bmatrix}, \quad \mathbf{r} = \begin{bmatrix} \mathbf{r}^f(\mathbf{u}^f; \mathbf{z}(\mathbf{u}^s)) \\ \mathbf{r}^s(\mathbf{u}^s; \mathbf{t}(\mathbf{u}^f)) \end{bmatrix}, \quad \mathbf{M} = \begin{bmatrix} \mathbf{M}^f & \mathbf{0} \\ \mathbf{0} & \mathbf{M}^s \end{bmatrix}, \tag{14}$$

where $\mathbf{u}$ is a combined vector of the fluid and structural states, and $\mathbf{z}$ and $\mathbf{t}$ denote the terms in the residual responsible for the coupling of the two subsystems. From Eq. 11, the residual of the structural subsystem may be separated as

$$\mathbf{r}^s(\mathbf{u}^s; \mathbf{t}(\mathbf{u}^f)) = \mathbf{r}^{ss}(\mathbf{u}^s) + \mathbf{r}^{sf}(\mathbf{t}(\mathbf{u}^f)). \tag{15}$$

The first term represents the effect of the current structural state, while the second term represents the effect of the traction, $\mathbf{t}$, from the fluid. Since the second term is linear in $\mathbf{t}$, a predicted value of the traction is introduced, $\tilde{\mathbf{t}}$, as presented in Froehle and Persson.[15] Thus, the residual can be re-written as

$$\mathbf{r}^s(\mathbf{u}^s;\mathbf{t}(\mathbf{u}^s)) = \mathbf{r}^s(\mathbf{u}^s;\tilde{\mathbf{t}}) + \mathbf{r}^{sf}(\mathbf{t}(\mathbf{u}^f) - \tilde{\mathbf{t}}). \tag{16}$$

Using the above formulation, Eq. 13 can be split as

$$\mathbf{M}\frac{\mathrm{d}\mathbf{u}}{\mathrm{d}t} = \begin{bmatrix} \mathbf{0} \\ \mathbf{r}^{sf}(\mathbf{t}(\mathbf{u}^f) - \tilde{\mathbf{t}}) \end{bmatrix} + \begin{bmatrix} \mathbf{r}^f(\mathbf{u}^f;\mathbf{z}(\mathbf{u}^s)) \\ \mathbf{r}^s(\mathbf{u}^s;\tilde{\mathbf{t}}) \end{bmatrix}. \tag{17}$$

With the introduction of a predictor, the coupled problem has been suitably modified into a form where the high-order IMEX scheme can be applied. As already mentioned, in the IMEX scheme the non-stiff (first) term is integrated explicitly and the stiff (second) term is integrated implicitly in time. However, the scheme differs slightly from IMEX as the evaluation of the explicit terms $\mathbf{r}^{sf}$ is avoided and instead the stage flux is updated for the structure equation using the corrected value of the coupling $\mathbf{t}(\mathbf{u}^f)$. To solve the subsystems implicitly, ESDIRK4, is employed. An explicit traction predictor, proposed by Van Zuijlen et al.,[4] for the structural subsystem, at an implicit stage i is given by

$$\tilde{\mathbf{t}} = \sum_{j=1}^{i-1} \frac{\hat{a}_{ij} - a_{ij}}{a_{ii}} \mathbf{t}_j, \tag{18}$$

where $\mathbf{t}_j$ is the traction at an intermediate stage j and $\hat{a}_{ij}$ and a_{ij} are the coefficients of the explicit and implicit Runge-Kutta integration schemes, respectively.

IV. Output-Based Mesh Adaptation

In the coupled FSI problem, the numerical error in the output results from discretization errors generated in both the fluid and structural subsystems. These errors are estimated and are used to drive the adaptation process. In this work, the primary focus of the adaptation will be on the fluid mesh. To adapt the mesh, spatially discrete but continuous in time adjoints are used to estimate the error in the output of interest.[16]

IV.A. Continuous-in-Time Adjoint Evaluation

Consider an unsteady output of the form

$$\bar{J} = \int_0^T J(\mathbf{U}^f, \mathbf{U}^s, t)\, dt + J_T(\mathbf{U}^f, \mathbf{U}^s), \tag{19}$$

where J and J_T are spatial functionals of the fluid, $\mathbf{U}^f$, and structural, $\mathbf{U}^s$, states. Note that J_T is a function of only the final-time (T) state. The continuous adjoints, $\mathbf{\Psi}^f$ and $\mathbf{\Psi}^s$, represent the sensitivities of the output to perturbations in the unsteady residuals $\bar{\mathbf{R}}^f$ (Eq. 8) and $\bar{\mathbf{R}}^s$ (Eq. 11), respectively. To derive the adjoint equations, a Lagrangian is defined as

$$\mathcal{L} = \bar{J} + \int_0^T \mathbf{\Psi}^{f,T}\bar{\mathbf{R}}^f dt + \int_0^T \mathbf{\Psi}^{s,T}\bar{\mathbf{R}}^s dt. \tag{20}$$

Substituting Eq. 19 into Eq. 20, integrating the second and third term by parts, and requiring stationarity of the Lagrangian with respect to the fluid state variations gives

$$\frac{\partial J_T}{\partial \mathbf{U}^f}\delta\mathbf{U}^f\Big|_{t=T} + \mathbf{\Psi}^{f,T}\mathbf{M}^f\delta\mathbf{U}^f\Big|_{t=T} - \mathbf{\Psi}^{f,T}\mathbf{M}^f\delta\mathbf{U}^f\Big|_{t=0} + \int_0^T \left[\frac{\partial J}{\partial \mathbf{U}^f} - \frac{\mathrm{d}\mathbf{\Psi}^{f,T}}{\mathrm{d}t}\mathbf{M}^f - \mathbf{\Psi}^{f,T}\frac{\partial \mathbf{r}^f}{\partial \mathbf{U}^f} - \mathbf{\Psi}^{s,T}\frac{\partial \mathbf{r}^s}{\partial \mathbf{U}^f}\right]\delta\mathbf{U}^f dt = \mathbf{0}. \tag{21}$$

The middle term at $t = 0$ drops out since the initial condition on the primal fully constrains the state there, so $\delta \mathbf{U}^f = 0$ at $t = 0$. The remaining terms yield the fluid adjoint differential equation (from the time integrand, transposed),

$$\mathbf{M}^f \frac{\mathrm{d}\boldsymbol{\Psi}^f}{\mathrm{d}t} + \frac{\partial \mathbf{r}^{f,T}}{\partial \mathbf{U}^f}\boldsymbol{\Psi}^f + \frac{\partial \mathbf{r}^{s,T}}{\partial \mathbf{U}^f}\boldsymbol{\Psi}_s = \frac{\partial J^T}{\partial \mathbf{U}^f}, \tag{22}$$

and the terminal condition

$$\boldsymbol{\Psi}^f(T) = -[\mathbf{M}^f]^{-1} \frac{\partial J_T}{\partial \mathbf{U}^f}\Big|_{t=T}. \tag{23}$$

The governing equations for the structural adjoint can be obtained in a similar fashion as well. As both the adjoint equations of the individual subsystems are coupled, they can be written in a matrix form as

$$\begin{bmatrix} \mathbf{M}^f & \mathbf{0} \\ \mathbf{0} & \mathbf{M}^s \end{bmatrix} \begin{bmatrix} \dot{\boldsymbol{\Psi}}^f \\ \dot{\boldsymbol{\Psi}}^s \end{bmatrix} + \begin{bmatrix} \dfrac{\partial \mathbf{r}^{f,T}}{\partial \mathbf{U}^f} & \dfrac{\partial \mathbf{r}^{s,T}}{\partial \mathbf{U}^f} \\ \dfrac{\partial \mathbf{r}^{f,T}}{\partial \mathbf{U}^s} & \dfrac{\partial \mathbf{r}^{s,T}}{\partial \mathbf{U}^s} \end{bmatrix} \begin{bmatrix} \boldsymbol{\Psi}^f \\ \boldsymbol{\Psi}^s \end{bmatrix} = \begin{bmatrix} \dfrac{\partial J^T}{\partial \mathbf{U}^f} \\ \dfrac{\partial J^T}{\partial \mathbf{U}^s} \end{bmatrix}. \tag{24}$$

The off-diagonal terms $\partial \mathbf{r}^{s,T}/\partial \mathbf{U}^f$ and $\partial \mathbf{r}^{f,T}/\partial \mathbf{U}^s$, which represent the change in the structural residual due to perturbation in the fluid state and the change in the fluid residual due to perturbation in the structural state, are evaluated using finite differences in this work. Due to the terminal condition, the adjoint equations are solved backward in time. The time integration scheme used for both the primal and the adjoint equation for this study is ESDIRK4 but other time schemes can be used as well.

IV.B. Error Estimation

The unsteady adjoint can be used to evaluate the error in the output of interest through the adjoint-weighted residual.[17] Let $\mathbf{U}_H^f$ be the approximate fluid solution obtained from the current space-time approximation space denoted by subscript H, and $\boldsymbol{\Psi}_{f,h}^T$ be the fluid adjoint in the fine space denoted by h. The error in the output is defined as:

$$\delta J = J_H(\mathbf{U}_H^f) - J_h(\mathbf{U}_h^f) \approx \frac{\partial J_h}{\partial \mathbf{U}_h^f}\delta \mathbf{U}_h^f \approx -\int_0^T \boldsymbol{\Psi}_h^{f,T} \bar{\mathbf{R}}_h^f(\mathbf{U}_H^f) dt, \tag{25}$$

where $\delta \mathbf{U}_h^f = \mathbf{U}_h^{f,H} - \mathbf{U}_h^f$ is the primal error in the fluid state and $\mathbf{U}_h^{f,H}$ is the injected solution from space H to h. The exact unsteady adjoint, which is unavailable, is approximated in a finer space grid by increasing the degrees of freedom in the spatial discretization. The finer space grid is obtained by increasing the spatial order of the elements by one in the fluid mesh.

IV.C. Fluid Mesh Adaptation

Unsteady error estimates in the space-time fluid mesh guide the adaptation process. Space-time elements selected for refinement or coarsening are chosed based on two factors: 1) estimated error in the space-time element, 2) computational cost of refinement. These two factors are combined into an adaptive indicator called the "figure of merit" which is the element error eliminated by refinement divided by the degrees of freedom introduced by the refinement. The cost, C, is defined by the total degrees of freedom,

$$C \equiv C^{\text{space}} C^{\text{time}} \quad , \quad C^{\text{space}} \equiv \sum_{e=1}^{N_e} n(p_e) \quad , \quad C^{\text{time}} \equiv N_t n_r, \tag{26}$$

where $n(p_e)$ is the number of spatial degrees for an element of order p_e, and n_r is the number of temporal degrees of freedom, i.e. system solves, per time step. For example, ESDIRK4 has $n_r = 5$. In this work the adaptive strategy refines in space by spatial order refinement (p-adaptation), and in time by reducing the uniform time step.

V. Numerical Results

In this section, the coupled adjoint is verified for two-dimensional FSI problems for varying outputs of interest. Using error estimates based the coupled adjoint, the efficiency of the adapted space-time meshes is demonstrated for fluid and structural outputs of interest. A pitching-plunging airfoil subjected to a high Reynolds number flow and a cantilever beam subjected to a laminar flow are the test cases of varying structural and fluid complexity, chosen to illustrate the benefits of mesh adaptivity in aeroelastic problems.

V.A. Pitching-plunging NACA 0012 airfoil

A two-dimensional pitching-plunging airfoil is a common aeroelastic model which has been studied extensively.[18] Consider a NACA 0012 airfoil pinned at the elastic axis in a free-stream flow of Mach number M_∞ as shown in Figure 2. The two degrees of freedom of the airfoil are the plunge h, which is taken to be positive in the downward direction, and the pitch angle α, which is considered positive clockwise (pitch up). The geometric properties of the airfoil are the chord c and semi-chord b. Measured from the nose of the airfoil, the center of mass and the elastic axis are located at x_{cg} and x_f, respectively. The inertia properties of the airfoil are the mass, m, and the moment of inertia about the elastic axis, I_f. The airfoil is connected to two springs at the elastic axis where the plunge spring represents the bending stiffness, K_h, of the structure, and the torsional spring represents the torsional stiffness, K_α. The equations of motion of the pitching-plunging airfoil are given as:

$$m\ddot{h} + S\ddot{\alpha} + K_h h = -L, \tag{27}$$

$$S\ddot{h} + I_f\ddot{\alpha} + K_\alpha \alpha = \tilde{M}, \tag{28}$$

where S is the static unbalance defined by the product between $(x_{cg} - x_f)$ and the mass of the airfoil, L is the total lift acting on the airfoil, and $\tilde{M}$ is the net aerodynamic moment on the airfoil about the elastic axis. The non-dimensional parameters used to describe the model are defined as:

$$\mu = \frac{m}{\pi\rho_\infty b^2}, \quad \bar{\omega} = \frac{\omega_h}{\omega_\alpha}, \quad r_\alpha = \sqrt{\frac{I_f}{mb^2}}, \quad \chi = \frac{S}{mb}, \tag{29}$$

where μ is the mass ratio, $\bar{\omega}$ is the ratio of the uncoupled natural frequencies, and r_α and χ are the non-dimensional inertia and static balance, respectively. The natural pitching and plunging frequencies are defined as $\omega_h = \sqrt{K_h/m}$ and $\omega_\alpha = \sqrt{K_\alpha/I_f}$. The case setup has been taken from Sanchez et al.[19] where the non-dimensional parameters are set as $\mu = 100$, $\bar{\omega} = 0.3185$, $r_\alpha = 0.5$ and $\chi = 0.25$, to ensure a subsonic flutter. The pitching frequency is set to be $\omega_\alpha = 45$ rad/s and the elastic axis is located at the quarter chord of the airfoil. The Mach number is $M_\infty = 0.345$, and the chord is $c = 1$. The airfoil is set at an initial angle of attack of five degrees to the flow.

A coarse, unstructured, triangular, viscous fluid mesh with 2766 elements is generated for the coupled simulation, as shown in Figure 3. The airfoil is located in the center of the domain, the boundary of which consists of a square box which spans from $[-100c, 100c]$ in both dimensions. The fluid flow is simulated using a RANS solver with the SA turbulence model.[20] The coupled system uses the fourth-order time scheme,

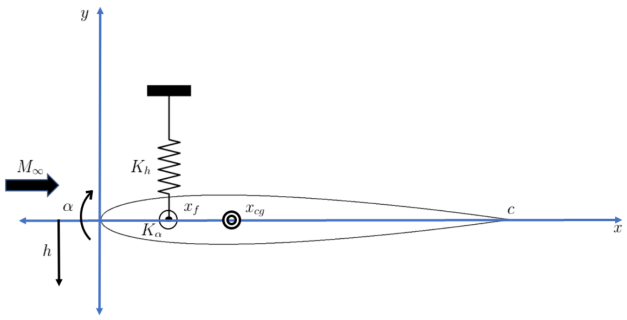

Figure 2: Model of a two-degree-of-freedom pitching-plunging airfoil.

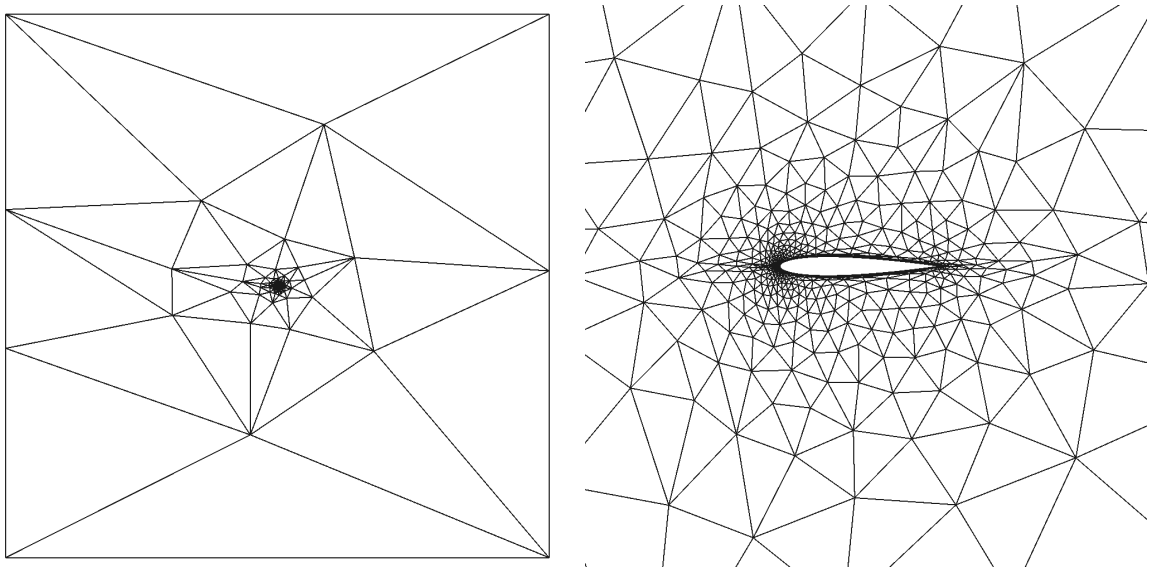

(a) (b)

Figure 3: Unstructured viscous mesh for the pitching-plunging airfoil test.

ESDIRK4, introduced in Section III, to march forward in time. A steady-state flow solution is used as the initial condition for the simulation. A mesh motion algorithm is applied to handle the deformations occurring in the fluid subsystem due to the moving airfoil. The mesh motion algorithm divides the spatial domain into two sub-domains. The region extending up to a radial distance of one chord away from the elastic axis is deformed rigidly according to the deformation provided by the structures solver. Following the region of rigid deformation, a septic polynomial blends the deformation smoothly in the region extending between a radial distance of one chord and two chords resulting in zero deformation at a radial distance of two chords.

The aeroelastic response of this coupled solver has been verified previously in Ojha et al.[21] To verify the coupled adjoint, a smooth laminar flow with a Reynolds number of $Re = 1000$ is simulated for five time steps with a final time of 0.005. The unsteady simulation is only run for a few such time steps to reduce the error arising from the temporal discretization. With this case setup, the unsteady coupled adjoint is verified by comparing the sensitivities of the outputs of interest against finite differences. Two outputs of interest from both the fluid and the structural subsystem are chosen: the time integrated lift and the pitch displacement and the final time lift and the pitch displacement. Using the adjoint formulation, the sensitives of the outputs of interest are evaluated with respect to the initial pitch angle of attack, which is set at time $t = 0$,

$$\frac{\partial J}{\partial \mathbf{U}^s}\bigg|_{t=0} = \mathbf{\Psi}^{s,T}\mathbf{M}^s\bigg|_{t=0}. \tag{30}$$

To evaluate the sensitivities from finite differences, a perturbation is given to the initial pitch angle of attack and the four outputs of interest are then evaluated again. The differences between the outputs in the perturbed condition and the original condition are used to evaluate the sensitivities. For the chosen outputs of interest, the agreement is excellent for small perturbations, as shown in Figure 4. The spatial order of interpolation is taken to be one for verification; however, similar agreement is obtained for higher spatial orders of interpolation as well. This verifies the implementation of the coupled adjoint in the FSI solver.

The verified coupled adjoint can be used in adapting the fluid and structural meshes for various outputs of interest, as shown in Section IV. In this work, the focus is on adapting fluid meshes for both fluid and structural outputs of interest. For mesh adaptation, the case setup is slightly changed, and a turbulent flow at a Reynolds number of $Re = 4 \times 10^6$ is used. At this flow condition, the Mach number of $M = 0.345$ is slightly below the flutter boundary of the structure and large oscillations are observed in the structure which damp in time. The fluid mesh is adapted for the time-integrated lift coefficient and time-averaged pitch displacement from time $t = 0$ to $t = 30$, during which the airfoil undergoes one complete pitch oscillation.

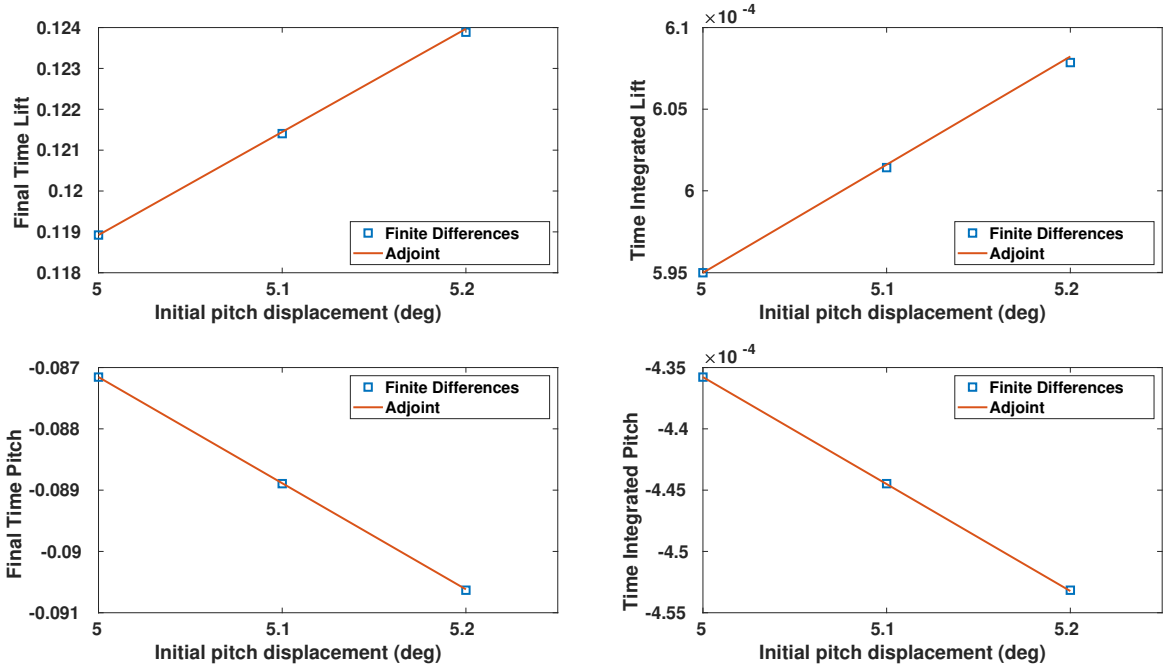

Figure 4: Verification of the coupled adjoint using a parameter sensitivity test.

Figure 5 shows the conservation of the x-momentum and y-momentum components of the fluid adjoint at the initial time. The magnitude of the fluid adjoint decreases away from the airfoil, showing that the output is most sensitive to the residuals on the elements above and below the airfoil, especially close to the trailing edge. The coupled adjoint detects the streamlines enveloping the structure as well as the regions in the mesh which are affected by the motion of the airfoil. Using the coupled adjoint, an unsteady error estimate for the output is evaluated and used to adapt the fluid mesh. The errors in the coupled output arise due to the spatial discretization errors in the fluid subsystem and the temporal discretization in both the fluid and the structural subsystem. A p-refinement study of the coupled simulation corroborated the effects of spatial discretization on the output for the two-degree of freedom system. An equivalent time-refinement study did not result in a significant change due to the fourth-order order time scheme, ESDIRK4, and a small time step used in the coupled simulation. Therefore, the spatial discretization errors dominate the output evaluation and an adaptive procedure is used to obtain an optimized fluid mesh. The total number of degrees of freedom introduced after each adaptive iteration is set by the growth factor which is $\mathrm{f_{tot}} = 1.2$. The optimized mesh is obtained by subjecting the coarse mesh to four cycles of p-adaptation.

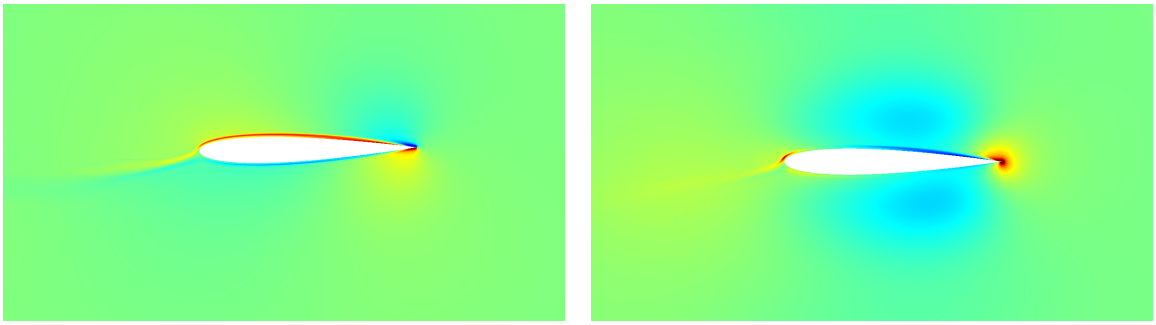

(a) Conservation of the x-momentum adjoint (b) Conservation of the y-momentum adjoint

Figure 5: Coupled adjoint solution for time-averaged pitch displacement output at the initial time.

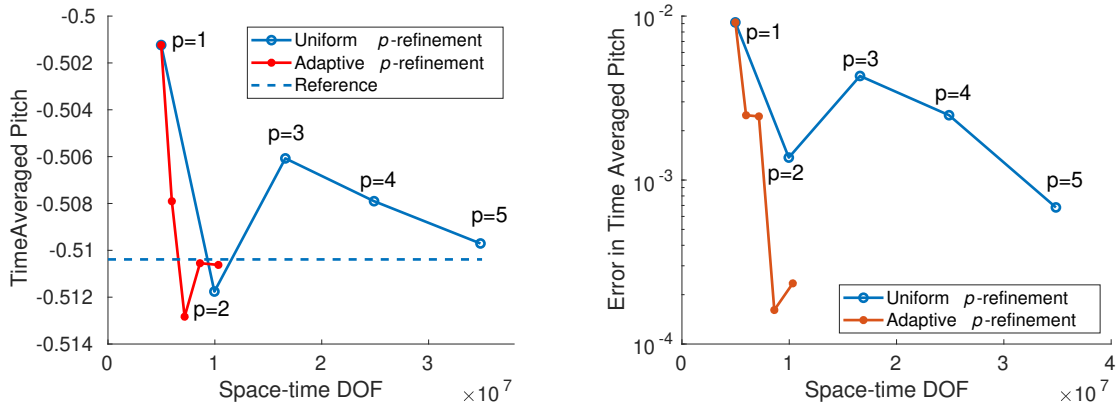

(a) Pitch convergence (b) Error convergence

Figure 6: Comparison of the time-averaged pitch for output-based adaptation to uniform-refinement.

Figure 7 shows the spatial order of interpolation post-adaptation. The higher order elements ($p = 4$ and $p = 5$) introduced in the adaptation process are those with the highest error estimates and lie primarily in the vicinity of the airfoil and inside the blending region. Goal-oriented adaptation using an uncoupled fluid adjoint for FSI problems is unable to capture the elements directly above and below the airfoil,[21] which are important for the structural subsystem, thus showcasing the importance of using the coupled adjoint for goal-oriented adaptation in FSI simulations. Figure 6 compares the convergence of the time-averaged pitch displacement for the adapted meshes against uniform p-refinement. At every stage of uniform refinement, the spatial order of the elements in the entire domain is increased by one. The reference/truth output, is evaluated with $p = 6$ elements in the entire spatial domain. The plot shows the effectiveness of the adaptation process relative to uniform refinement. Figure 6 also compares the error in pitch displacement for the adapted meshes against uniform p-refinement. The adapted meshes converge at a faster rate with fewer degrees of freedom, thereby increasing accuracy and reducing computational cost. These advantages can also be seen when a similar mesh adaptation study conducted is for a fluid output of interest, the time averaged

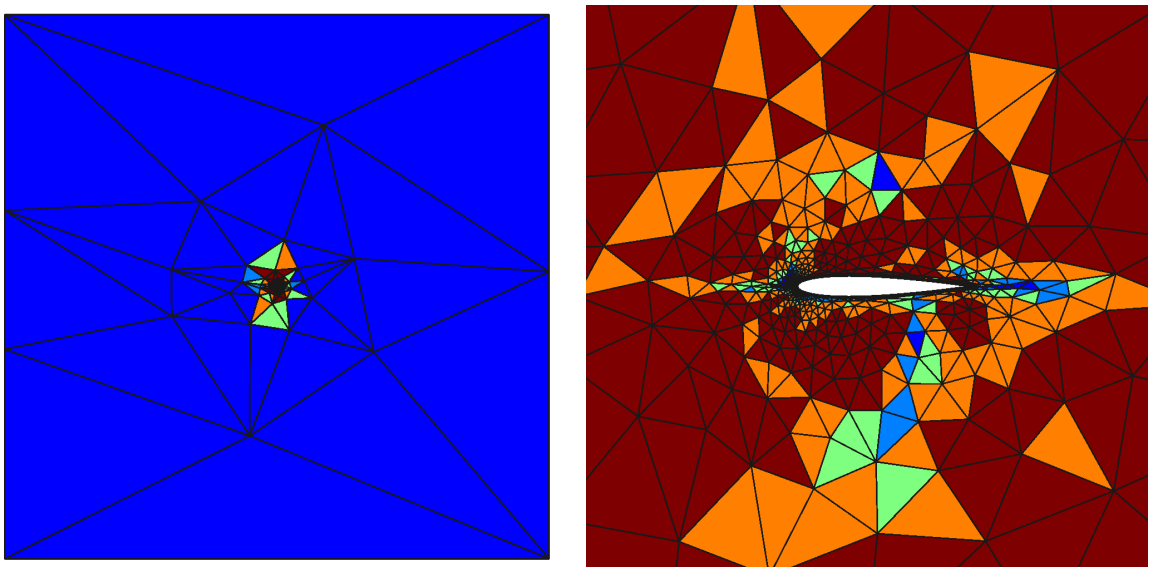

(a) (b)

Figure 7: Element order distribution at the end of the adaptation process for the pitching-plunging airfoil. Dark blue denotes $p = 1$, light blue denotes $p = 2$, green denotes $p = 3$, oranges denote $p = 4$, and dark red denotes $p = 5$ order elements.

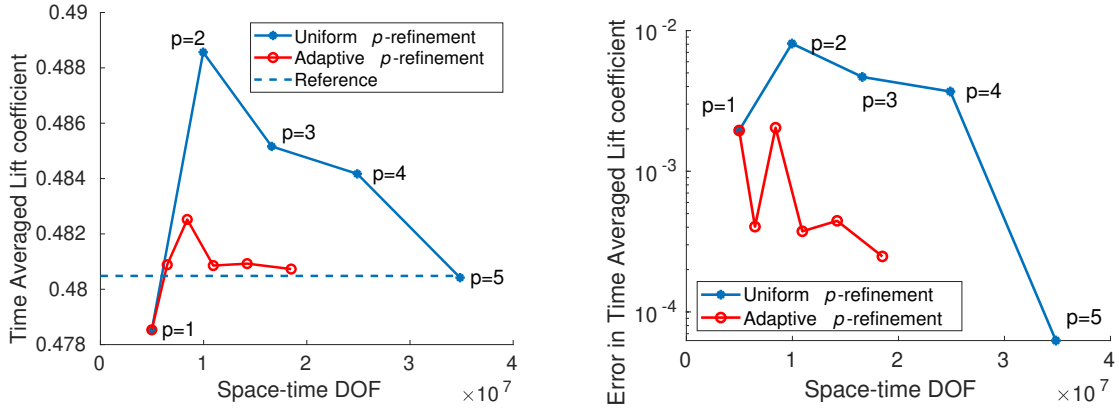

(a) Lift convergence (b) Error convergence

Figure 8: Comparison of the time-averaged lift coefficient for output-based adaptation to uniform-refinement.

lift coefficient as shown in Figure 8.

V.B. Cantilever Beam

Consider the flow around an Euler-Bernoulli beam cantilevered at the leading edge. At the undeformed strain-free position, the beam makes an angle of attack of 5 degrees to the flow. The actual beam is considered two dimensional when represented in the fluid mesh, with a length of 1 and a thickness of 0.005. The fluid mesh is represented by an unstructured square grid consisting of 758 nodes and 871 triangular elements. The domain extends up to a distance of 100 chords from the beam, which is cantilevered at the center of the domain. Free-stream boundary conditions are applied at the outer boundary of the mesh. The planar beam is represented by 16 beam finite elements of uniform size in the structural solver. The cantilever beam is subjected to a uniform fluid flow with a Mach number of $M_\infty = 0.345$ and Reynolds number of $Re = 1000$. The Euler-Bernoulli beam has a bending stiffness $EI = 0.2$ and mass per unit length $m = 1$. The beam element has two nodes with two degrees of freedom per node. Proportional damping in the form of Rayleigh damping with parameters, $\alpha = 1$ and $\beta = 1$ is used to model the structure. The equations of motion for the cantilever beam are given as

$$\bar{\mathbf{M}}\ddot{\mathbf{u}}^s + \mathbf{C}\dot{\mathbf{u}}^s + \mathbf{K}\mathbf{u}^s = \mathbf{F}, \tag{31}$$

where $\mathbf{u}^s$ is the displacement at a particular node, $\bar{\mathbf{M}}$ is the mass matrix, $\mathbf{K}$ is the stiffness matrix, $\mathbf{C}$ is the Rayleigh damping matrix and $\mathbf{F}$ is the force vector. At time $t = 0$, the structure is at rest and the fluid state is obtained from a steady solve for the steady state solution of the fluid. $p = 1$ order polynomials have been used for the fluid spatial discretization and the time scheme for both subsystems is ESDIRK4. The two subsystems are coupled temporally using the IMEX scheme.

To verify the coupled adjoint, a smooth laminar flow with a Reynolds number of $Re = 1000$ is simulated for a single time step with a final time $T = 0.0001s$. The unsteady coupled adjoint is verified by comparing the sensitivities of the outputs of interest with respect to the initial shape of the beam against finite differences. Two outputs of interest from both the fluid and the structural subsystem are chosen: (i) the time integrated lift and the tip displacement, and (ii) the final time lift and the tip displacement. The initial shape of the beam at $t = 0$ is given by

$$u^s\Big|_{t=0} = A\sin(x), \tag{32}$$

where the amplitude variable, A, is perturbed. Using the adjoint formulation, the sensitives of the outputs of interest are evaluated with respect to the initial shape of the beam, set at time $t = 0$. Using the adjoints, the sensitivities are given as

$$\frac{\partial J}{\partial \mathbf{U}^s}\Big|_{t=0} = \mathbf{\Psi}^{s,T}\bar{\mathbf{M}}\Big|_{t=0} - \dot{\mathbf{\Psi}}^{s,T}\mathbf{C}\Big|_{t=0}. \tag{33}$$

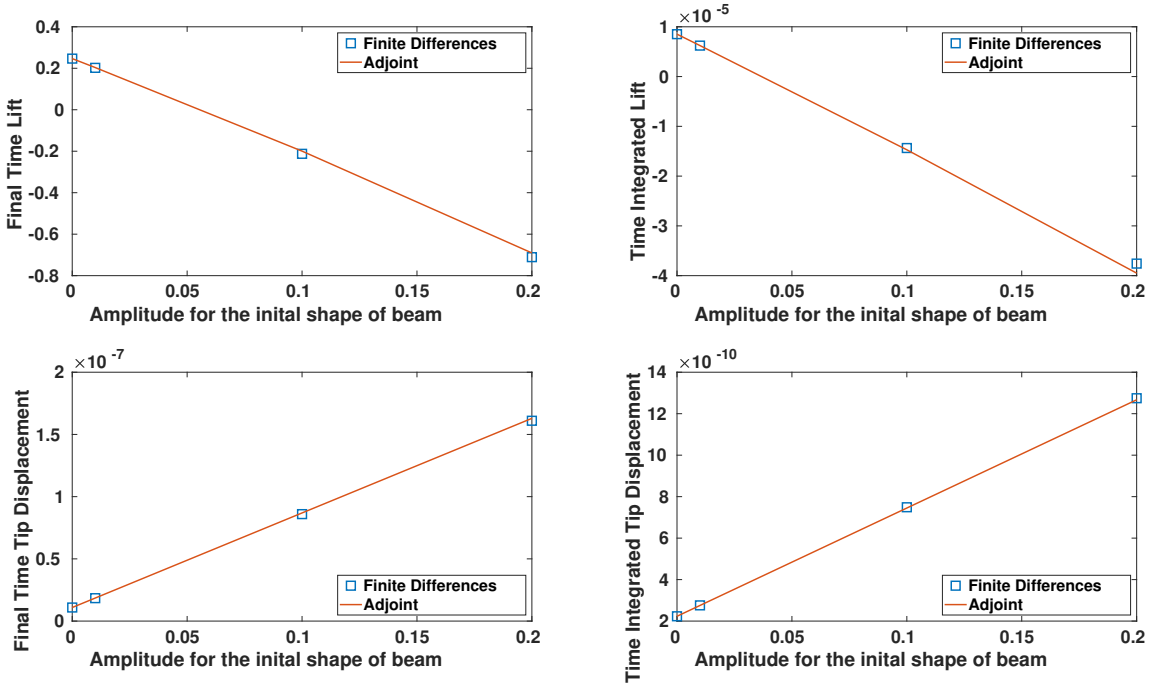

Figure 9: Verification of the coupled adjoint using a parameter sensitivity test.

To evaluate the sensitivities from finite differences, a perturbation is given to the amplitude variable, A, and the four outputs of interest are then evaluated again. The differences between the outputs in the perturbed condition and the original condition are used to evaluate the sensitivities. For the chosen outputs of interest, the agreement is excellent for small perturbations, as shown in Figure 9, and it verifies the implementation of the beam coupled adjoint.

Having verified the coupled adjoint, an error estimate based on the coupled adjoint is used to adapt the fluid meshes for coupled outputs of interest. For mesh adaptation, the case setup described above is simulated for a longer duration, with a final time of 4 using 200 uniform timesteps. The fluid mesh is firstly adapted for a time averaged lift coefficient. Figure 10 shows the conservation of x-momentum and y-momentum components of the fluid adjoint at initial time. The sensitivity of the output by the flow at the trailing edge of the beam is highlighted by the fluid adjoint. The structural adjoint, a one dimensional field in this case, also showcases higher sensitivity of the output to the structural degrees of freedom at the trailing edge. The trailing edge is important for defining the overall camber of the beam which in turn dictates the total lift generated. Thus, the increased sensitivity of the output to the trailing edge is expected

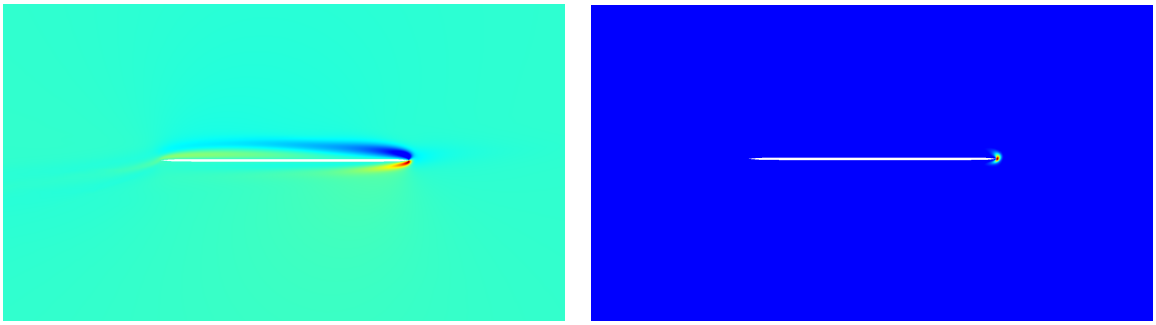

(a) Conservation of the x-momentum adjoint (b) Conservation of the y-momentum adjoint

Figure 10: Coupled adjoint solution for time-averaged lift coefficient output at the initial time.

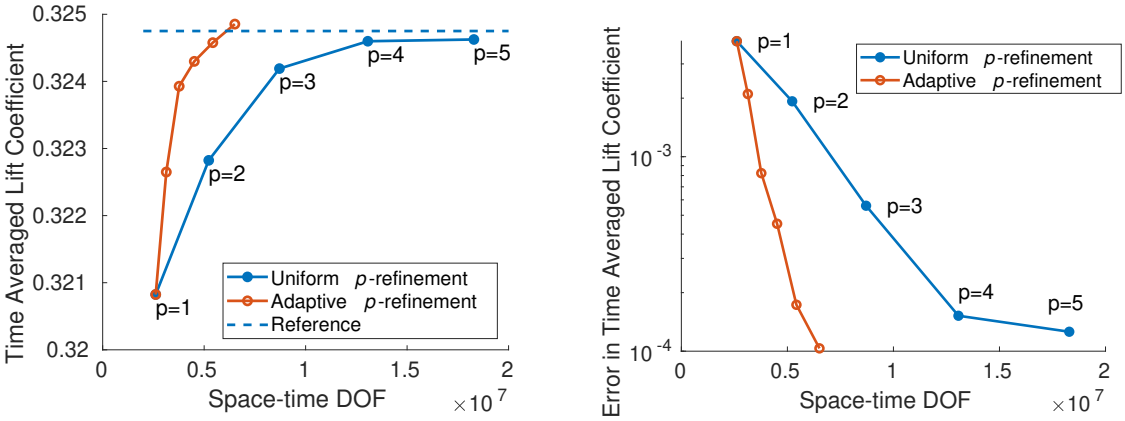

(a) Lift convergence (b) Error convergence

Figure 11: Comparison of the time-averaged lift coefficient for output-based adaptation to uniform-refinement.

and captured well by the coupled adjoint. The initial fluid mesh, with uniform $p = 1$ elements in the entire domain, is subjected to five cycles of mesh adaptation, with a growth factor of $f_{tot} = 1.2$. Figure 12 shows the spatial order distribution post adaptation. The mesh adaptation targets elements in the fluid mesh undergoing mesh deformation along with those elements highlighted by the adjoint, i.e above and below the beam. A comparison of the output convergence between the adapted meshes against uniform p-refined meshes is shown in Figure 11. The output evaluated for a uniform $p = 6$ mesh serves as the reference output and is used for evaluating the errors. A similar output convergence study is also conducted for a structural output, the time-integrated tip displacement, as shown in Figure 13. For the structural output of interest, the previously-used growth factor of $f_{tot} = 1.2$ was insufficient to reduce errors significantly and was subsequently increased to $f_{tot} = 1.3$. This delayed convergence for the tip displacement output of interest can be attributed to the way mesh refinement and mesh adaption are executed in this study. For structural outputs of interest, the discretization errors arising from the structural mesh could be more dominant than

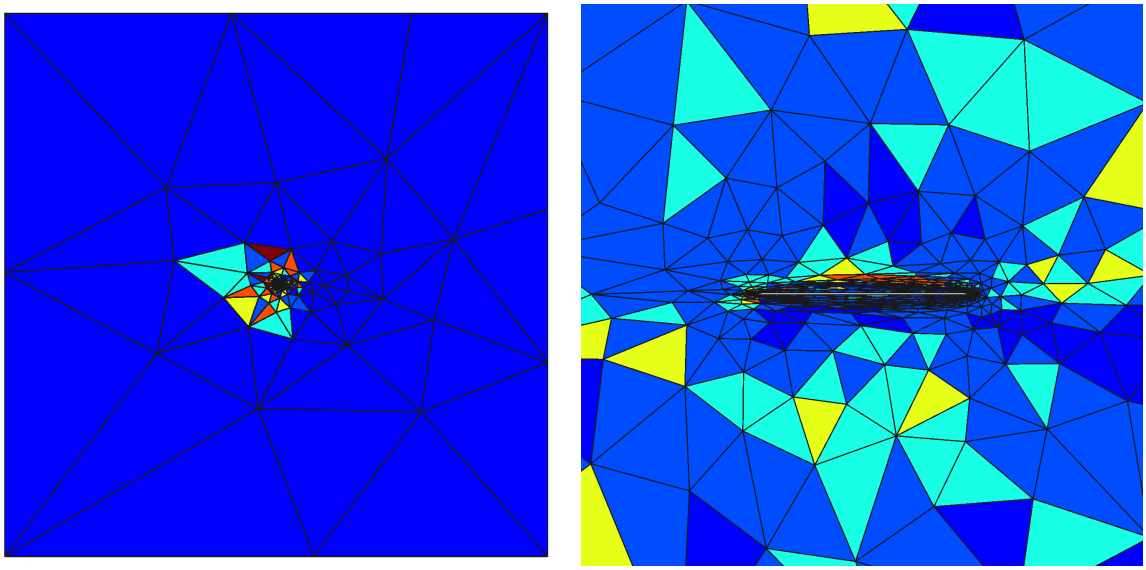

(a) (b)

Figure 12: Element order distribution at the end of the adaptation process for the pitching-plunging airfoil. Dark blue denotes $p = 1$, light blue denotes $p = 2$, green denotes $p = 3$, oranges denote $p = 4$, and dark red denotes $p = 5$ order elements.

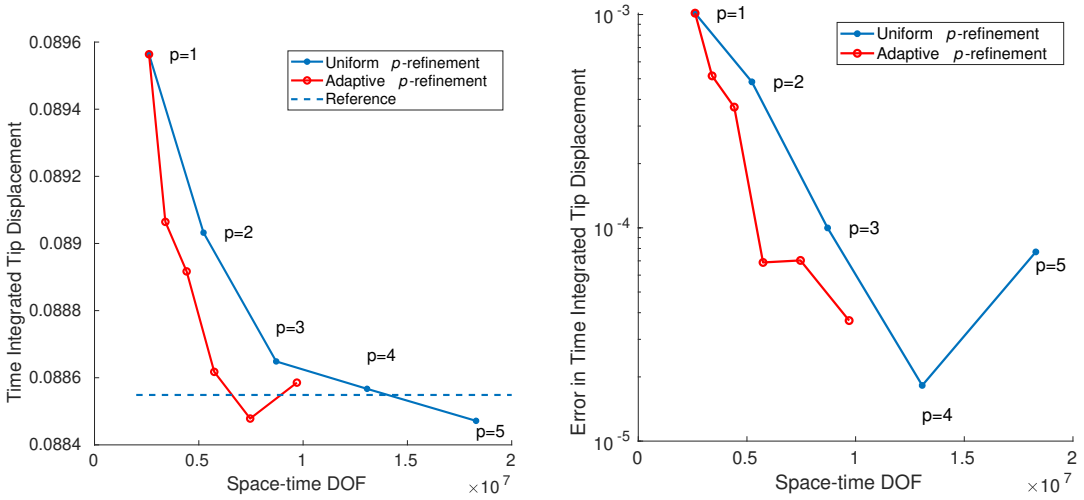

(a) Displacement convergence (b) Error convergence

Figure 13: Comparison of the time-integrated beam tip displacement for output-based adaptation to uniform-refinement.

those arising from the fluid mesh, particularly at later stages of fluid mesh refinement. Without mesh refinement or mesh adaption occurring in the structural subsystem, these errors arising from the structural discretization persist and affect the outputs, leading to delayed convergence. Despite the source of dominant error, the adapted meshes are able to reduce the error in a similar fashion as uniform $p-$refinement. The advantages of adaptive meshing can be seen clearly for both outputs of interest where convergence is achieved with fewer degrees of freedom. Mesh adaptation using the coupled adjoint on both subsystems is expected to give even better convergence rates and more savings on computational cost.

VI. Concluding Remarks

In the paper, the concept of goal-oriented mesh adaptation is applied successfully using a coupled adjoint for fluid-structure interaction problems of varying complexity. The coupled adjoint is verified for a two-dimensional pitching-plunging NACA 0012 airfoil subjected to a subsonic flow and a cantilever beam subjected to a laminar flow. An adaptive meshing procedure based on the coupled adjoint is applied to the fluid mesh to obtain accurate time-averaged coupled outputs. The adaptive meshing procedure adapts in regions important to both subsystems and helps in obtaining accurate outputs at smaller number of degrees of freedom. Overall, the adaptive meshing procedure provides a significant increase in the accuracy of unsteady outputs for aeroelastic problems compared to more common adaptation methods, such as uniform refinement. The development of the coupled adjoint extends the applicability of output-based mesh adaptation to both the fluid and structural subsystems. This extension of mesh-adaptation capability to adapt in both subsystems is the subject of ongoing research. Future work will explore the most efficient way of dividing the total degrees of freedom in the complete FSI system for accurate evaluation of coupled outputs.

Acknowledgments

This work is supported by the U.S. Air Force Research Laboratory (AFRL) under the Michigan-AFRL Collaborative Center in Aerospace Vehicle Design (CCAVD), with Dr. Philip Beran as the task Technical Monitor.

References

[1]Afonso, F., Vale, J., Oliveira, É., Lau, F., and Suleman, A., "A review on non-linear aeroelasticity of high aspect-ratio wings," *Progress in Aerospace Sciences*, Vol. 89, 2017, pp. 40–57.

[2]Hou, G., Wang, J., and Layton, A., "Numerical methods for fluid-structure interaction—a review," *Communications in Computational Physics*, Vol. 12, No. 2, 2012, pp. 337–377.

[3]Hübner, B., Walhorn, E., and Dinkler, D., "A monolithic approach to fluid–structure interaction using space–time finite elements," *Computer methods in applied mechanics and engineering*, Vol. 193, No. 23-26, 2004, pp. 2087–2104.

[4]van Zuijlen, A. H., de Boer, A., and Bijl, H., "Higher-order Time Integration Through Smooth Mesh Deformation for 3D Fluid-structure Interaction Simulations," *J. Comput. Phys.*, Vol. 224, No. 1, May 2007, pp. 414–430.

[5]Fidkowski, K. J. and Darmofal, D. L., "Review of Output-Based Error Estimation and Mesh Adaptation in Computational Fluid Dynamics," *American Institute of Aeronautics and Astronautics Journal*, Vol. 49, No. 4, 2011, pp. 673–694.

[6]van der Zee, K., van Brummelen, E., Akkerman, I., and de Borst, R., "Goal-oriented error estimation and adaptivity for fluid–structure interaction using exact linearized adjoints," *Computer Methods in Applied Mechanics and Engineering*, Vol. 200, No. 37-40, Sept. 2011, pp. 2738–2757.

[7]Persson, P.-O., Bonet, J., and Peraire, J., "Discontinuous Galerkin solution of the Navier–Stokes equations on deformable domains," *Computer Methods in Applied Mechanics and Engineering*, Vol. 198, No. 17-20, 2009, pp. 1585–1595.

[8]Kast, S. M. and Fidkowski, K. J., "Output-based Mesh Adaptation for High Order Navier-Stokes Simulations on Deformable Domains," *Journal of Computational Physics*, Vol. 252, No. 1, 2013, pp. 468–494.

[9]Cockburn, B., Karniadakis, G. E., and Shu, C.-W., *Discontinuous Galerkin methods: theory, computation and applications*, Vol. 11, Springer Science & Business Media, 2012.

[10]Reed, W. H. and Hill, T., "Triangular mesh methods for the neutron transport equation," Tech. rep., Los Alamos Scientific Lab., N. Mex.(USA), 1973.

[11]Fidkowski, K. J., Oliver, T. A., Lu, J., and Darmofal, D. L., "p-Multigrid solution of high–order discontinuous Galerkin discretizations of the compressible Navier-Stokes equations," *Journal of Computational Physics*, Vol. 207, 2005, pp. 92–113.

[12]Smith, M. J., Cesnik, C. E. S., and Hodges, D. H., "Evaluation of Some Data Transfer Algorithms for Noncontiguous Meshes," *Journal of Aerospace Engineering*, Vol. 13, No. 2, 2000, pp. 52–58.

[13]Persson, P.-O., Peraire, J., and Bonet, J., "A high order discontinuous Galerkin method for fluid-structure interaction," *18th AIAA Computational Fluid Dynamics Conference*, 2007, p. 4327.

[14]Wendland, H., "Konstruktion und Untersuchung radialer Basisfunktionen mit kompaktem Träger," *Göttingen, Georg-August-Universität zu Göttingen, Diss*, 1996.

[15]Froehle, B. and Persson, P.-O., "A high-order discontinuous Galerkin method for fluid–structure interaction with efficient implicit–explicit time stepping," *Journal of Computational Physics*, Vol. 272, 2014, pp. 455–470.

[16]Fidkowski, K. J., "Output-Based Space-Time Mesh Optimization for Unsteady Flows Using Continuous-in-Time Adjoints," *Journal of Computational Physics*, Vol. 341, No. 15, July 2017, pp. 258–277.

[17]Fidkowski, K. J. and Darmofal, D. L., "Review of Output-Based Error Estimation and Mesh Adaptation in Computational Fluid Dynamics," *American Institute of Aeronautics and Astronautics Journal*, Vol. 49, No. 4, 2011, pp. 673–694.

[18]Bisplinghoff, R. L., Ashley, H., and Halfman, R. L., *Aeroelasticity*, Courier Corporation, 2013.

[19]Sanchez, R., L. Kline, H., Thomas, D., Variyar, A., Righi, M., Economon, T., Alonso, J., Palacios, R., Dimitriadis, G., and Terrapon, V., "Assessment of the fluid-structure interaction capabilities for aeronautical applications of the open-source solver SU2." 01 2016, pp. 1498–1529.

[20]Ceze, M. A. and Fidkowski, K. J., "High-order output-based adaptive simulations of turbulent flow in two mineaviationdimensions," *AIAA Journal*, Vol. 54, No. 9, 2016.

[21]Ojha, V., Fidkowski, K., and Cesnik, C. E. S., "High-Fidelity Coupled Fluid-Structure Interaction Simulations with Adaptive Meshing," *AIAA Aviation 2019 Forum*, 2019, p. 3056.